A Finite-Difference Scheme for Three-Dimensional Incompressible Flows in Cylindrical Coordinates

R. Verzicco and P. Orlandi

Dipartimento di Meccanica e Aeronautica Università di Roma "La Sapienza," Via Eudossiana 18, 00184 Rome, Italia

A finite-difference scheme for the direct simulation of the incompressible time-dependent three-dimensional Navier-Stokes equations in cylindrical coordinates is presented. The equations in primitive variables (v_r, v_θ, v_z and p) are solved by a fractional-step method together with an approximate-factorization technique. Cylindrical coordinates are singular at the axis; the introduction of the radial flux $q_r = r \cdot v_r$, on a staggered grid simplifies the treatment of the region at $r = 0$. The method is tested by comparing the evolution of a free vortex ring and its collision with a wall with the theory, experiments, and other numerical results. The formation of a tripolar vortex, where the highest vorticity is at $r = 0$, is also considered. Finally to emphasize the accurate treatment near the axis, the motion of a Lamb dipole crossing the origin is simulated. © 1996 Academic Press, Inc.

1. INTRODUCTION

In recent years, thanks largely to direct simulation, great advances have been made in the comprehension of transitional and turbulent wall-bounded and free-shear flows. The studies have been limited mainly to planar boundaries due to the ease afforded by Cartesian coordinates. Transitional boundary layers [1], turbulent channel flows [2], and plane mixing layers [3] are examples of such flows.

Many interesting flows, however, require cylindrical coordinates even if some of them can be solved in Cartesian coordinates but to the detriment of accuracy. For example, Melander *et al.* [4] performed the simulation of a three-dimensional round jet in Cartesian coordinates with reasonable results, but the periodic boundary conditions introduced an unphysical perturbation with $n = 4$ azimuthal wavenumber.

In Cartesian coordinates, within simple boundary conditions, very efficient and accurate spectral methods have been developed. The development of an efficient spectral method in cylindrical coordinates requires a large effort to approximate the radial derivatives and to treat the singularity at $r = 0$. Stanaway *et al.* [5] used spectral methods for axisymmetric flows by introducing special functions for the radial derivatives. The complexity of the scheme is illustrated by the statement of the authors

that 128×128 modes required a memory larger than the in-core memory of a CRAY-XMP48. Leonard *et al.* [6] proposed an accurate method for three-dimensional pipe flows with Jacobi polynomials for the radial direction. These polynomials were introduced to minimize the coupling of the momentum equations, nevertheless the discretization produced large nondiagonal sparse matrices to be inverted. Buell *et al.* [7] developed a Galerkin method to simulate the natural convection in a circular enclosure. In the radial direction Bessel functions were used and the condition of finiteness of the solution was applied at $r = 0$. However, the Galerkin method was used to reduce the linearized perturbation equations to an eigenvalue problem and no information was provided about the extension of the method to the full Navier–Stokes equations.

A finite volume method was employed by Eggels [8] for LES in a turbulent pipe. The radial momentum equation required an extended gridvolume at the axis to avoid the evaluation of quantities at $r = 0$. For the same reason, extrapolations and first-order-accurate differences were used at the axis with a reduction of the overall accuracy. Nevertheless, in the pipe the decreased accuracy was assumed to be not significant due to the smooth behavior of the flow near the centerline.

Finite-differences are generally less accurate than spectral methods but, on the other hand, they have the advantage of being very flexible for complex geometries and boundary conditions. Due to this property it has recently been shown that finite-differences are good candidates for direct simulation of complex flows, especially when global conservation properties are maintained. Rai *et al.* [9] and Choi *et al.* [10] performed this check for the direct simulation of the channel flow, showing that low order statistics are adequately described by second-order schemes while higher accuracies (fourth or fifth order) are required for high-order statistics. For laminar flows, in particular, second-order accuracy is satisfactory (see [11]) and many interesting problems requiring cylindrical coordinates, such as round jets [12] and swirling flows can be properly studied. For Cartesian

402

coordinates many examples of second-order finite-difference schemes are available in literature; in contrast, presumably due to the singularity at $r = 0$ almost no examples are found for cylindrical coordinates. Schumann [13] developed a finite-difference scheme in cylindrical coordinates for the simulation of turbulent flows in annuli, but in that case the flow was confined between two cylinders and the singularity at $r = 0$ was not encountered.

In this paper a finite-difference scheme for three-dimensional incompressible time-dependent flows in cylindrical coordinates is presented. The scheme, based on a fractional-step and approximate-factorization technique, is second-order accurate in space and time. The major difficulty arises from the singularity of the Navier–Stokes equations at $r = 0$. The introduction of the quantity $q_r = r\, v_r$, on a staggered grid simplifies the discretization of this region since $q_r \equiv 0$ at $r = 0$. The scheme is designed to solve wall-bounded as well as free-shear flows with only minor changes in the procedure, and an example will be given in Section 5.

The stability and accuracy of the method has been validated by comparing the evolution of an axisymmetric vortex ring with that obtained by a vorticity–streamfunction scheme valid for axisymmetric flows. The functional relationship characteristic of the steady translating solution has been calculated. When azimuthal perturbations are introduced, these are amplified, at sufficiently high Reynolds number, by the self-induced mean strain as described by Widnall *et al.* [14]. The numerical results correctly predicted the most unstable wavenumber (n^*) obtained by the linear stability theory [14], as well as the growth of a band of modes around n^* [15]. The accuracy of the method was shown by the good agreement between the growth rate of n^* and that of the linear theory. To test the feasibility of the method to solve flows in presence of walls, we simulated the collision of a vortex ring with a wall and the same features as in the experiment of Walker *et al.* [16] were observed. In particular, the trajectories of the centers of primary, secondary, and tertiary vortices agreed very well with those measured.

The vortex ring has a very small amount of vorticity near the axis; hence, as a severe test of the treatment of the region around $r = 0$, the case of a tripole formation is considered. This flow has been solved in the $r - \theta$ plane and compared with that obtained in Cartesian coordinates [17]. In this flow an accurate discretization near the origin is required since the peak vorticity is located at $r = 0$. A more extreme test of the treatment at the axis is given by the crossing of a Lamb dipole through the origin. This flow is not axisymmetric and with the largest velocities occurring at $r = 0$, where there are also the smallest computational cells. Even if this is one of the worst applications for polar coordinates, the present method maintains stability and retains the second-order accuracy for all the velocity components.

2. GOVERNING EQUATIONS

The incompressible Navier–Stokes and continuity equations are rewritten with the quantities $q_\theta = v_\theta$, $q_r = r \cdot v_r$, and $q_z = v_z$. In this way the continuity equation assumes a form similar to that in Cartesian coordinates:

$$\frac{\partial q_r}{\partial r} + \frac{\partial q_\theta}{\partial \theta} + r\,\frac{\partial q_z}{\partial z} = 0. \tag{1a}$$

In terms of the q_i the momentum equations in conservative form become

$$\frac{Dq_\theta}{Dt} = -\frac{1}{r}\frac{\partial p}{\partial \theta} + \frac{1}{\mathrm{Re}}\left[\frac{1}{r}\left(\frac{\partial}{\partial r} r \frac{\partial q_\theta}{\partial r}\right) - \frac{q_\theta}{r^2} + \frac{1}{r^2}\frac{\partial^2 q_\theta}{\partial \theta^2}\right.$$
$$\left. + \frac{\partial^2 q_\theta}{\partial z^2} + \frac{2}{r^3}\frac{\partial q_r}{\partial \theta}\right],$$

$$\frac{Dq_r}{Dt} = -r\frac{\partial p}{\partial r} + \frac{1}{\mathrm{Re}}\left[r\frac{\partial}{\partial r}\left(\frac{1}{r}\frac{\partial q_r}{\partial r}\right) + \frac{1}{r^2}\frac{\partial^2 q_r}{\partial \theta^2}\right. \tag{1b}$$
$$\left. + \frac{\partial^2 q_r}{\partial z^2} - \frac{2}{r}\frac{\partial q_\theta}{\partial \theta}\right],$$

$$\frac{Dq_z}{Dt} = -\frac{\partial p}{\partial z} + \frac{1}{\mathrm{Re}}\left[\frac{1}{r}\frac{\partial}{\partial r}\left(r\frac{\partial q_z}{\partial r}\right) + \frac{1}{r^2}\frac{\partial^2 q_z}{\partial \theta^2} + \frac{\partial^2 q_z}{\partial z^2}\right],$$

with

$$\frac{Dq_\theta}{Dt} \equiv \frac{\partial q_\theta}{\partial t} + \frac{1}{r^2}\frac{\partial r q_\theta q_r}{\partial r} + \frac{1}{r}\frac{\partial q_\theta^2}{\partial \theta} + \frac{\partial q_\theta q_z}{\partial z},$$

$$\frac{Dq_r}{Dt} \equiv \frac{\partial q_r}{\partial t} + \frac{\partial}{\partial r}\left(\frac{q_r^2}{r}\right) + \frac{\partial}{\partial \theta}\left(\frac{q_\theta q_r}{r}\right) + \frac{\partial q_r q_z}{\partial z} - q_\theta^2, \tag{1c}$$

$$\frac{Dq_z}{Dt} \equiv \frac{\partial q_z}{\partial t} + \frac{1}{r}\frac{\partial q_r q_z}{\partial r} + \frac{1}{r}\frac{\partial q_\theta q_z}{\partial \theta} + \frac{\partial q_z^2}{\partial z},$$

where in the q_θ equation the following identities have been used:

$$\frac{1}{r}\left(\frac{\partial}{\partial r} r \frac{\partial q_\theta}{\partial r}\right) - \frac{q_\theta}{r^2} = \frac{\partial}{\partial r}\left(\frac{1}{r}\frac{\partial r q_\theta}{\partial r}\right), \tag{1d}$$

$$\frac{1}{r^2}\frac{\partial r q_\theta q_r}{\partial r} = \frac{1}{r}\frac{\partial q_\theta q_r}{\partial r} + \frac{q_\theta q_r}{r^2}. \tag{1e}$$

A characteristic length r_0 and a circulation Γ give the velocity scale (Γ/r_0) and the pressure scale ($\rho\, \Gamma^2/r_0^2$). The Reynolds number is $\mathrm{Re} = \Gamma/\nu$, with ν being the kinematic viscosity.

The advantages of the conservative form for the nonlinear terms were emphasized, for two-dimensional flows,

in the precursor paper by Arakawa [18] for the $\psi - \omega$ formulation, and successively extended to the primitive variables by Grammelwedt [19]. Horiuti [20] also showed that the conservative form minimizes, especially near the wall, the truncation errors associated with central second-order finite differences. This is a very important requirement in wall-bounded flows.

The scheme can be applied to flows radially bounded by free-slip or no-slip walls. In the z direction both periodic or wall-bounded flows can be considered with only minor changes in the numerical procedure. Due to the use of trigonometric expansions in the pressure correction solver (see Section 3) the method at the moment is limited to uniform grids in θ and z while a nonuniform grid can be used in the radial direction. This limitation forces the use of a large number of gridpoints in θ and z to have a fine mesh instead of allowing clustering only in certain regions. However, the extension to nonuniform grids in all three directions is now feasible since very efficient multigrid algorithms to solve elliptic equations in complex regions are available [10].

3. NUMERICAL METHOD

The time-advancement of Eq. (1) employs a fractional-step method extensively described in [21, 9]. However, since by introducing the pressure at the old time step, the boundary conditions for the intermediate velocity field $\hat{\mathbf{q}}$ are simplified (N. N. Mansour, *personal communication*) we wish to shortly summarize the equations to show the small differences. The third-order low-storage Runge–Kutta in combination with the Crank–Nicolson scheme, described in Ref. [9] is used to evaluate the nonsolenoidal velocity field $\hat{\mathbf{q}}$:

$$\frac{\hat{q}_i - q_i^l}{\Delta t} = \left[\gamma_l H_i^l + \rho_l H_i^{l-1} - \alpha_l \mathscr{G}_i p^l + \alpha_l (A_{i\theta} + A_{ir} + A_{iz}) \frac{(\hat{q}_i + q_i^l)}{2} \right]. \tag{2}$$

H_i contains the convective terms and those viscous terms with a single velocity derivative, $\mathscr{G}_i$, $A_{i\theta}$, and A_{iz} denote discrete differential relations for the pressure and viscous terms, respectively, whose explicit expressions are easily obtained by straightforward central second-order finite differences. α_l, γ_l, and ρ_l are the coefficients of the time advancement scheme and the same values as [9] have been used. The implicit treatment of the viscous terms of Eq. (2) would require for the solution the inversion of large sparse matrices, these are reduced to three tridiagonal matrices by a factorization procedure with error $O(\Delta t^3)$ [22]. By using the increment $\Delta \hat{q}_i = \hat{q}_i - \hat{q}_i^l$ Eq. (2) can be written in delta form, giving

$$(1 - \beta_l A_{i\theta})(1 - \beta_l A_{iz})(1 - \beta_l A_{ir}) \Delta \hat{q}_i$$
$$= \Delta t \left[\gamma_l H^l + \rho_l H^{l-1} - \alpha_l \mathscr{G}_i p^l \right. \tag{3}$$
$$+ \alpha_l (A_{i\theta} + A_{ir} + A_{iz}) q_i^l],$$

with $\beta_l = \alpha_l \Delta t/2$. The solution requires boundary conditions for $\hat{\mathbf{q}}$ and a procedure similar to that suggested in [21] yields for the nonsolenoidal field $\hat{q}_i = q_i^{l+1} + O(\Delta t^2)$ (see Appendix A1).

The intermediate velocity field $\hat{\mathbf{q}}$ must be globally free-divergent, but not locally. The continuity equation is then enforced on each cell by

$$q_i^{l+1} - \hat{q}_i = -\alpha_l \Delta t \mathscr{G}_i \Phi^{l+1}, \tag{4}$$

where Φ is a scalar calculated from

$$\mathscr{L} \Phi^{l+1} = + \frac{1}{\alpha_l \Delta t} \mathscr{D} \hat{\mathbf{q}}, \tag{5}$$

In Eq. (5) $\mathscr{D}$ and $\mathscr{L} = \mathscr{D}\mathscr{G}$ indicate the discrete differential relations

$$\mathscr{D} \cdot = \frac{1}{r} \frac{\delta \cdot}{\delta \theta} + \frac{1}{r} \frac{\delta \cdot}{\delta r} + \frac{\delta \cdot}{\delta z}, \quad \mathscr{L} \cdot = \frac{1}{r^2} \frac{\delta^2 \cdot}{\delta \theta^2} + \frac{1}{r} \frac{\delta}{\delta r} r \frac{\delta \cdot}{\delta r} + \frac{\delta^2 \cdot}{\delta z^2}. \tag{6}$$

On one side we can note that the dimensions of the terms of $\mathscr{D}$ are not the same; however, since it is applied to $\hat{\mathbf{q}}$ (with $\hat{q}_r = r \hat{v}_r$), the quantity $\mathscr{D} \hat{\mathbf{q}}$ has dimensionally correct terms.

We wish to point out that, differently from [9, 21] the introduction of the pressure p^l in Eq. (2) simplifies the boundary conditions for $\hat{\mathbf{q}}$ but, on the other hand, it requires the explicit calculation of the pressure gradients through $\mathscr{G} p^{l+1} = \mathscr{G} p^l + \mathscr{G} \Phi^{l+1} - (\alpha_l \Delta t/2\text{Re}) \mathscr{L}\mathscr{G}\Phi^{l+1}$.

The features of the third-order Runge–Kutta are well described in [23]; here we only stress that since $\rho_1 = 0$, each time step is self-starting and a variable Δt can be used without introducing interpolating procedures.

4. TREATMENT OF THE AXIS

The discretization of the region around $r = 0$ is the most important feature of the present scheme and, in our opinion, the difficulties in its accurate representation are the reason for the few simulations in literature. It might seem that in Eqs. (1) there are lots of singularities, however, the most are only apparent. In fact the advantage of using a staggered grid is that only the component q_r is evaluated at the grid point $j = 1$ ($r = 0$), and there $q_r =$
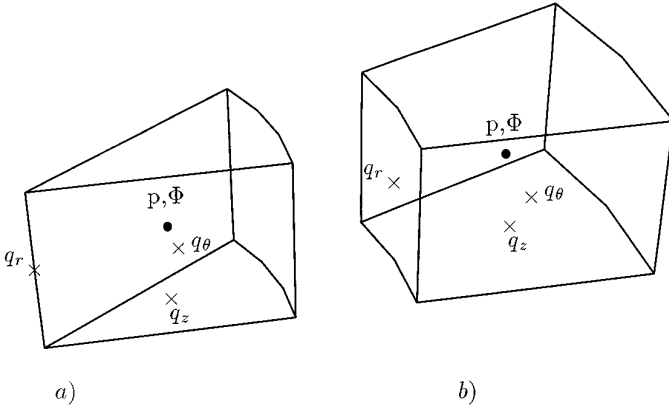
FIG. 1. Sketch of the computational cells: (a) cell at the axis; (b) cell in the domain.

0 by definition (Fig. 1). The equation for q_r can be then discretized for all $j \geq 2$ straightforwardly. A further advantage of using a staggered grid is that when q_θ is not zero at $r = 0$ (see, for example, Section 5.4), it switches signs at the origin; however, this singularity is automatically handled by this grid since the q_θ-equation is evolved only starting from the radial location $j = \frac{3}{2}$.

The equations for q_z and q_θ at $j = \frac{3}{2}$ require the evaluation of radial derivatives in the region around $r = 0$. The fact that $q_r \equiv 0$ at $j = 1$ avoids the evaluation of q_θ and q_z at $j = 1$ and the radial derivatives of the convective terms can be discretized without any approximation.

On the other hand, the viscous radial derivative for q_z is (only the radial indices are indicated):

$$\frac{1}{r}\frac{\delta}{\delta r} r \frac{\delta q_z}{\delta r}\bigg|_{j=3/2} = \frac{1}{r_{3/2}}\left[r_2 \frac{(q_z)_{5/2} - (q_z)_{3/2}}{\Delta r^2} \right], \qquad (7)$$

and the opportunity to have $r_1 \equiv 0$ avoids the approximation of $\delta q_z/\delta r|_{j=1}$ with a reduced accuracy. However, in the case of flows within annuli it results that $r_1 \neq 0$ and the radial derivative is discretized by first-order approximations as usually done in Cartesian coordinates [9].

The viscous derivative for q_θ can be written in two ways. The form on the right-hand side of Eq. (1d), usually found in textbooks, can be discretized only when it is expanded as

$$\frac{\partial}{\partial r}\frac{1}{r}\frac{\partial r q_\theta}{\partial r} = -\frac{1}{r^2}\frac{\partial r q_\theta}{\partial r} + \frac{1}{r}\frac{\partial^2 r q_\theta}{\partial r^2},$$

giving the discretized form

$$-\frac{1}{r^2}\frac{\delta r q_\theta}{\delta r} + \frac{1}{r}\frac{\delta^2 r q_\theta}{\delta r^2}\bigg|_{j=3/2}$$

$$= -\frac{1}{(r_{3/2})^2}\left[\frac{(q_\theta)_{5/2} + (q_\theta)_{3/2}}{2\Delta r} r_2 \right] \qquad (8a)$$

$$+ \frac{1}{r_{3/2}}\left[\frac{(r q_\theta)_{5/2} - (r q_\theta)_{3/2}}{\Delta r} - \frac{(r q_\theta)_{3/2} 2}{\Delta r} \right]\frac{1}{\Delta r}.$$

The evaluation of $(\delta r q_\theta/\delta r)|_{j=1}$ by a forward first-order accurate expression reduces the overall accuracy of the scheme. The reduced accuracy is not relevant in flows with negligible q_θ at the axis (vortex rings) but it is important when q_θ is present, even when it has a smooth profile.

The second expression is

$$\frac{1}{r}\frac{\delta}{\delta r} r \frac{\delta q_\theta}{\delta r} - \frac{q_\theta}{r^2}\bigg|_{j=3/2} \qquad (8b)$$

$$= \frac{1}{r_{3/2}}\left[r_2 \frac{(q_\theta)_{5/2} - (q_\theta)_{3/2}}{\Delta r} \right]\frac{1}{\Delta r} - \frac{(q_\theta)_{3/2}}{(r_{3/2})^2}.$$

Since in this case $r_1 \equiv 0$ no approximations have been done and the derivative maintains its second-order accuracy at the axis.[1] As a check for Eq. (8a) and Eq. (8b) we considered the axisymmetric vorticity distribution of an isolated monopole, given in [17], whose instability leads to the tripole formation (see Section 5.3)

$$\omega_z(r) = \left[1 - \frac{1}{2}\alpha\left(\frac{r}{\varrho}\right)^\alpha \right] e^{-(r/\varrho)^\alpha}, \qquad (9)$$

where α controls the steepness of the vorticity gradients and ϱ controls the size of the monopole. From the definition of ω_z at the axis $(\omega_z = (1/r)(\partial r q_\theta/\partial r))$ the viscous radial derivative for q_θ has been analytically computed and the results compared with those obtained by Eqs. (8a) and (8b). For $r \gg 0$ both expressions give identical results; on the contrary at $r = 0$ and in its neighbor large differences

---

[1] A third possible expression is

$$\frac{1}{r^2}\frac{\delta}{\delta r} r^3 \frac{\delta}{\delta r}\frac{q_\theta}{r}\bigg|_{j=3/2} = \frac{1}{(r_{3/2})^2}\left[(r_2)^3 \frac{(q_\theta/r)_{5/2} - (q_\theta/r)_{3/2}}{\Delta r} \right]\frac{1}{\Delta r}. \qquad (8c)$$

In this case the only assumption is $r^3 (\delta/\delta r)(q_\theta/r)|_{j=1} = 0$ and this is not true if $(\delta/\delta r)(q_\theta/r)|_{j=1} \to \infty$ as r^{-3}. However, it is not difficult to show that $r^3 \partial u_\theta/\partial r$ vanishes at the axis for a C^∞ velocity field. This is because as $r \to 0$, $u_\theta \sim r^{\|m\|-1}$ for the mth azimuthal Fourier mode provided $m \neq 0$ while for $m = 0$ we have $u_\theta \sim r$. This expression seems to be accurate as expression (8b) (see Fig. 2), and, in fact, for all cases simulated in the $(r - x)$-plane the same results have been obtained. For nonaxisymmetric cases, however, like that in Section 5.4 the expression (8b) gives the most accurate results and has to be used for full three-dimensional simulations.
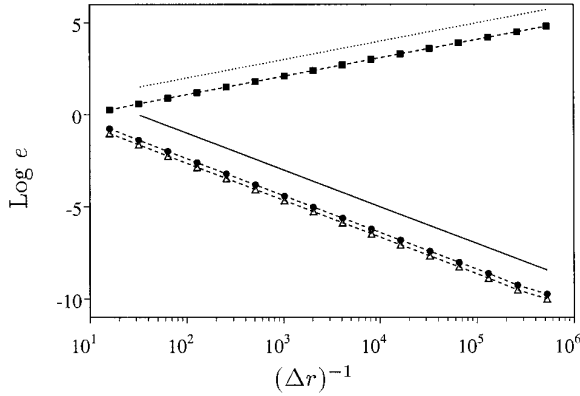
FIG. 2. Error of the viscous radial derivative at the axis vs $(\Delta r)^{-1}$ for the q_θ equation: ● expressions (8b), ■ expression (8a), △ expression (8c) (in the footnote), ——— slope -2, $\cdots$ slope $+1$. It has been used in Eq. (9), $\alpha = 3$ and $\rho = 1$.

arise. Figure 2 shows that, as expected, the error for the expression (8b) decreases as $(\Delta r)^2$ while the error increases as $1/\Delta r$ for the expression (8a). The reason for the undesirable behavior of Eq. (8a) is the following: due to the forward finite-difference at the axis, the error is $O(\Delta r)$, this error is then divided by Δr and then by $r_{3/2} \equiv \Delta r/2$, resulting in an overall error $O(1/\Delta r)$.

Finally we would like to mention the possibility of treating the azimuthal momentum equation like the radial, that is, solving an equation for the quantity $\tilde{q}_\theta = rv_\theta$. This has been done for some flows, obtaining results indistinguishable from the previous. Therefore, since the original set of unknowns (q_r, q_θ, q_z, p) requires less changes in the Navier–Stokes equations, we preferred to preserve this formulation. For the same reason the axial component of the momentum equation has been solved in terms of $q_z = v_z$, instead of $\tilde{q}_z = rv_z$. In fact, while, on one hand, $\tilde{q}_z$ renders the continuity equation (1a) identical to that in Cartesian coordinates, on the other hand, it would require

further changes in the Navier–Stokes equations without leading to any improvement of the results.

5. NUMERICAL RESULTS

In this section we present some applications of the scheme to different flows. Comparison with theoretical, experimental, and numerical results obtained by different methods are also shown to prove the qualities of the method.

5.1. Free Vortex Ring

The case of a free vortex ring is considered to check the ability of the method to simulate flows with axial velocity at $r = 0$. A thin ring with Gaussian vorticity translates with axial velocity [25],

$$V = \frac{\Gamma}{4\pi r_0}\left(\ln\frac{8r_0}{\hat{a}} - 0.558\right), \tag{10}$$

where r_0 is the toroidal radius, $\hat{a}^2(t) = (\hat{a}_o^2 + 4\nu t)^{1/2}$ is the instantaneous core radius, and Γ is the circulation. This expression rigorously holds if $\hat{a}(t)/r_0 \ll 1$ (thin core) with a correction term of $O((\hat{a}/r_0)^2 \ln(8r_0/\hat{a}(t)))$ [24].

We consider a Gaussian initial vorticity distribution

$$\omega_\theta = \frac{1}{\pi a_o^2} e^{s^2/a_o^2}, \quad s^2 \equiv (r - r_0)^2 + (z - z_0),$$

with r_0 and z_0 the coordinate of the center of the ring core. The vertical size of the domain was fixed at $6r_0$ and periodicity is assumed in this direction. The motion of the ring has been radially confined within a finite domain of radius $r_f = 4r_0$, where a free-slip condition has been imposed. The value of a_o was chosen to be 0.4131. At early times the computed speed of the ring agrees with (10).

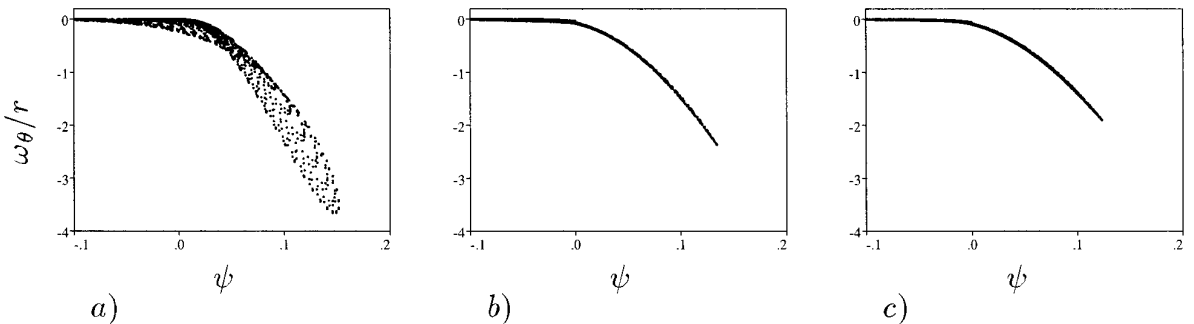Axisymmetric simulations have shown that the initial

FIG. 3. Scatter plots of vorticity vs Stokes streamfunction for the axisymmetric free vortex ring at Re = 5500: (a) $t = 0$; (b) $t = 60$; (c) $t = 100$.
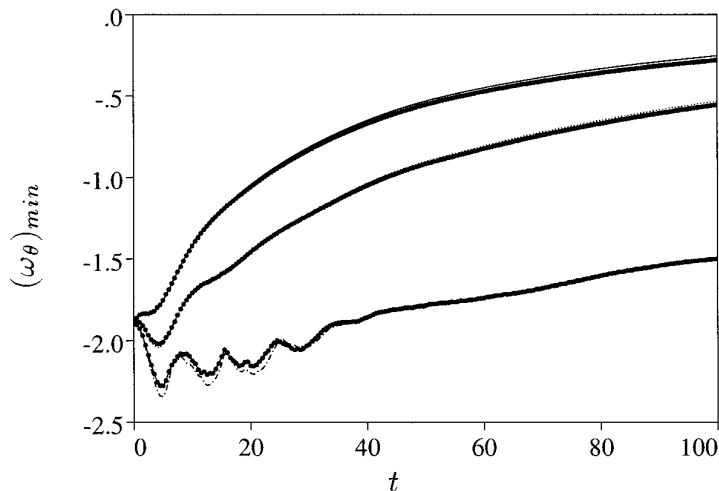
FIG. 4. Time evolution of the minimum vorticity for the axisymmetric free vortex ring. $\psi - \omega$ formulation: ——— Re = 500; $\cdots$ Re = 1000; $-\cdot-$ Re = 5500; ● present scheme. The grid is 128 × 128 in the radial and axial directions for both schemes.

stage of the evolution is characterized by the readjustment of the Gaussian vorticity distribution (Fig. 3a), which relaxes toward a single-value steady relationship $\omega_\theta/r = f(\psi)$ (Fig. 3b), where ψ is the Stokes streamfunction in a frame moving with the ring. The attainment of a single-value relationship indicates steady translation only for Re $\rightarrow \infty$; however, at high Reynolds number viscous diffusion produces a decrease of the peak vorticity without changing the functional relationship (Fig. 3c). Figure 4 shows the evolution of the peak vorticity for different Reynolds numbers and the results are compared with those obtained by an axisymmetric code in the $\omega - \psi$ formulation with the nonlinear terms discretized by the Arakawa [18] scheme. This scheme is especially made for axisymmetric flows since, in the limit Re $\rightarrow \infty$, it conserves the circulation and the quadratic invariants (energy and $\int (\omega_\theta/r)^2 \, dS$), ensuring that spurious vorticity is not generated [18]. On the other hand, the present method conserves only circulation and energy; hence, it is expected to show small differences from the other scheme at high Reynolds number when the viscosity does not diffuse some spurious vorticity.

This is confirmed by the discrepancies at Re = 5500, even if after the initial stage the oscillations caused by the vorticity readjustment are damped and both methods give the same results. It should be stressed, however, that the importance of the conservation of $\int (\omega/r)^2 \, dS$ arises only in axisymmetric flows since in three-dimensions only the energy is conserved and this holds in the present scheme. It might seem then that the present scheme becomes more accurate in three dimensions, due to the absence of some invariants, and, of course, it is not true. In fact, the minor precision of the three-dimensional scheme has to be interpreted only as a need of higher spatial resolution with respect to the axisymmetric scheme, where the invariants

are preserved automatically. On the other hand, when performing full three-dimensional simulations of unbounded flows the quality of the results is checked by monitoring the impulse which is very well preserved by the present scheme.

When a random radial displacement is imposed on the toroidal radius of the ring $r'(\theta) = r_0 [1 + \varepsilon(\theta)]$, the vortex ring develops azimuthal instabilities. According to the inviscid theory, the number of waves of the instability depends on the ratio of the core radius to ring radius and the specific distribution of vorticity. An alternate form of the core to ring radius ratio is the parameter $\tilde{V} \doteq V 4\pi r_0/\Gamma$. Widnall and Tsai [14] by a linear stability theory evaluated the most unstable wavenumber (n^*) as function of $\tilde{V}$ for a uniform vorticity core. Their result is also a close approximation for a Gaussian vorticity, provided that for the core size $\hat{a}$ required in the calculation of $\tilde{V}$ one uses the radius at which the maximum tangential velocity occurs, i.e., $\tilde{a} \simeq 1.121a$. This gives $\tilde{V} \simeq 2.6$. This parameter has also been calculated numerically from the translation velocity of the ring; the same value has been found both in the axisymmetric and in the full three-dimensional simulation $\tilde{V} = 2.47$. The linear stability theory and experiments [14] predict that for a ring with a continuous vorticity distribution and $\tilde{V}$ in the present range the most unstable wavenumber is $n^* = 6$.[2] Saffman [15] showed that each wavelength n^* is the center of a narrow band of unstable modes, the width of the band depending on the strain field induced by the ring. Figure 5a shows the time evolution

---

[2] A more correct way to obtain the number of waves is the following: for the Gaussian vortex the wavenumber of the second nonrotating mode is $ka_0 = (n/r_o)a_0 = 2.26$ [26] which gives $n = 5.47$. Since the number of waves must be an integer it is expected n to be 5 or 6.
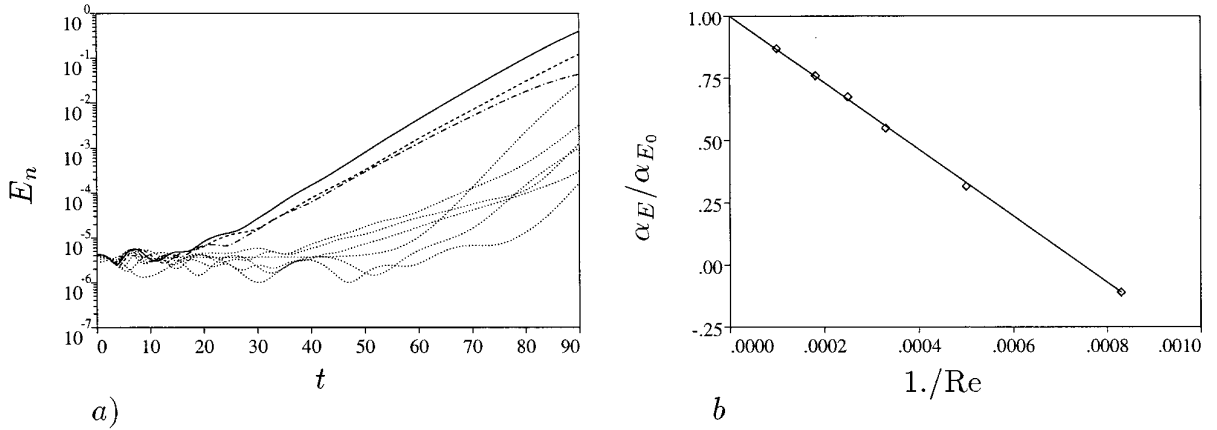
FIG. 5. (a) Time evolution of the azimuthal energy modes in the free vortex ring at Re = 5500 (97 × 97 × 129 grid): —— $n = 6$; ——— $n = 5$; —·— $n = 7$, ··· other modes. (b) Normalized growth-rate of the most amplified wavenumber vs inverse of the Reynolds number: ◇ numerical values; —— linear fitting.

of the energy azimuthal modes at Re = 5500. In agreement with the linear theory, $n = 6$ is the most unstable wavenumber and also the narrow band of unstable modes, suggested by Saffman, is confirmed by the growth of the modes $n = 5$ and $n = 7$. The growth rate of the $n = 6$ mode is $\alpha_E \simeq 0.09$, more than 20% smaller than the value α_{E_0} predicted by the linear theory [14]. The agreement seems rather poor but we should keep in mind that the theory is valid for stagnant waves in vortex rings with very thin cores in an inviscid fluid. Therefore, many factors might account for this difference: the core is not thin, the unstable waves may rotate in the strain-free case (the theory assumes stagnant waves), and the simulation is not inviscid. Performing the simulation for different Reynolds numbers, it is shown that the viscosity accounts the most of the difference and a simple one-term correction of the form $\alpha_E = \alpha_{E_0}(1 - \alpha_{E_1}/\text{Re})$ predicts the growth rate of the most unstable mode from the inviscid value up to the point of damping (Fig. 5b). α_{E_1} is the critical Reynolds number that, from a linear fitting of the data of Fig. 5b turns out to be Re = 1332. In Ref. [26] it is also shown that in order to make the correction independent of the core thickness of the ring, another Reynolds number, based on the self-induced strain, has to be used. A detailed description of the correction is beyond the scope of this paper, and it is given in [26].

5.2. Vortex Ring Colliding with a Wall

In order to show the capability of the method to simulate flows bounded in the axial direction, the same vortex ring has been considered for the collision with a wall. In this case the simulation was performed in a domain of vertical size $3.5r_0$ with a no-slip wall in the lower side and a free-slip wall in the upper. As in the previous example a free-slip wall was placed at $r_f = 4r_0$. In Ref. [16] the features of the collision were described and in Ref. [11] direct simulation was used to investigate the details of the interaction and to compare the numerical results with the experiments. Here we wish only to show a comparison with other numerical solutions and a grid-refinement check.

The main events of the interaction are shown in Fig. 6 with the formation of a secondary ring and the early appearance of a tertiary ring.

A simulation of the Navier–Stokes equations in primitive variables in the axisymmetric case at Re = 2895 has been performed to compare the results with the simulation in $\omega - \psi$ variables performed in [11]. In Fig. 6 the azimuthal vorticity field at $t = 30$, obtained by the same grids (129 × 129 and 257 × 513) used in [11] is shown and, as expected, the results are indistinguishable. In Fig. 7a peak vorticities obtained by the $\omega - \psi$ formulation of [11] (257 × 513 grid) and the present scheme (with the same grid) are compared.

The main aim of the next example is to show that a free-slip wall located at a convenient distance from the axis of symmetry approximates an infinite domain without requiring coordinate transformations to move the external boundary further away. To this purpose two calculations, with the same spacing as the 129 × 129 grid, are performed with $r_f = 8r_0$ (257 × 129 grid) and $r_f = 2r_0$ (65 × 129 grid). Figure 7b shows the time evolution of the minimum and maximum vorticities. The simulations by $r_f = 4r_0$ and $r_f = 8r_0$ do not differ, proving that with respect to the dynamics of the vortex–wall interaction, the radial boundary is at an infinite distance. On the contrary, the simulation by $r_f = 2r_0$ shows that the vorticities attain smaller values since the presence of a close free-slip boundary prevents the radial spreading of the structures and the vorticity undergoes a minor stretching.
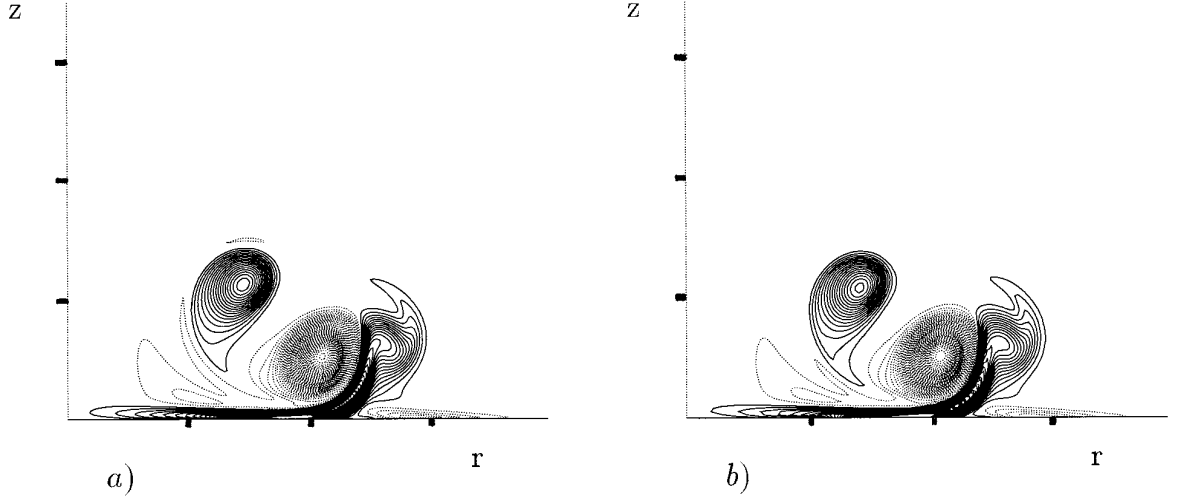
FIG. 6. Azimuthal vorticity field for a vortex ring impinging on a wall at Re = 2895 and $t = 30$: (a) 257×513 grid; (b) 129×129 grid; —— positive values; $\cdots$ negative values ($\Delta = \pm 0.05$). Tick marks at the axis are every x, $r = r_0$.
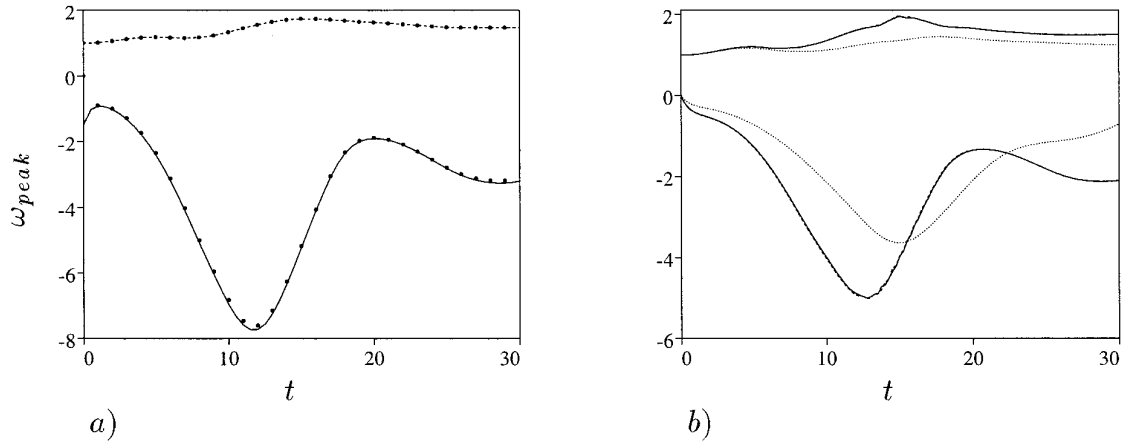

FIG. 7. Time evolution of the peak vorticities, normalized to the peak vorticity of the ring at $t = 0$, for the vortex ring impinging on a wall at Re = 2895. (a) (257×513 grid) $\omega - \psi$ formulation of [11]: —— ω_{min}; --- ω_{max}; ● present scheme. (b) —— $r_f = 4r_0$; --- $r_f = 8r_0$; $\cdots$ $r_f = 2r_0$.
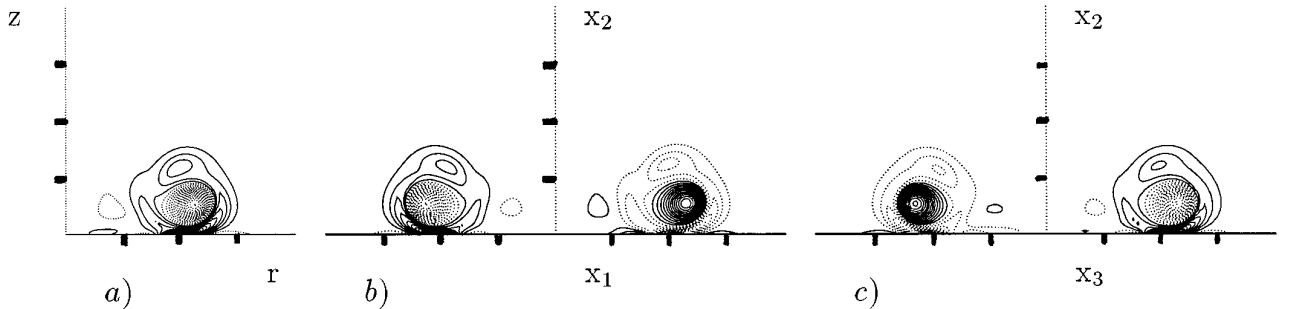

FIG. 8. Vorticity contour plots for a vortex ring impinging on a wall at Re = 1389 and $t = 48$. (a) azimuthal vorticity (cylindrical coordinates), (b) and (c) (Cartesian coordinates) ω_x and ω_z, respectively. —— positive values, $\cdots$ negative values ($\Delta = \pm 0.05$). Tick marks are every r_0. In these simulations the axial extension of the computational domain was $4r_0$.
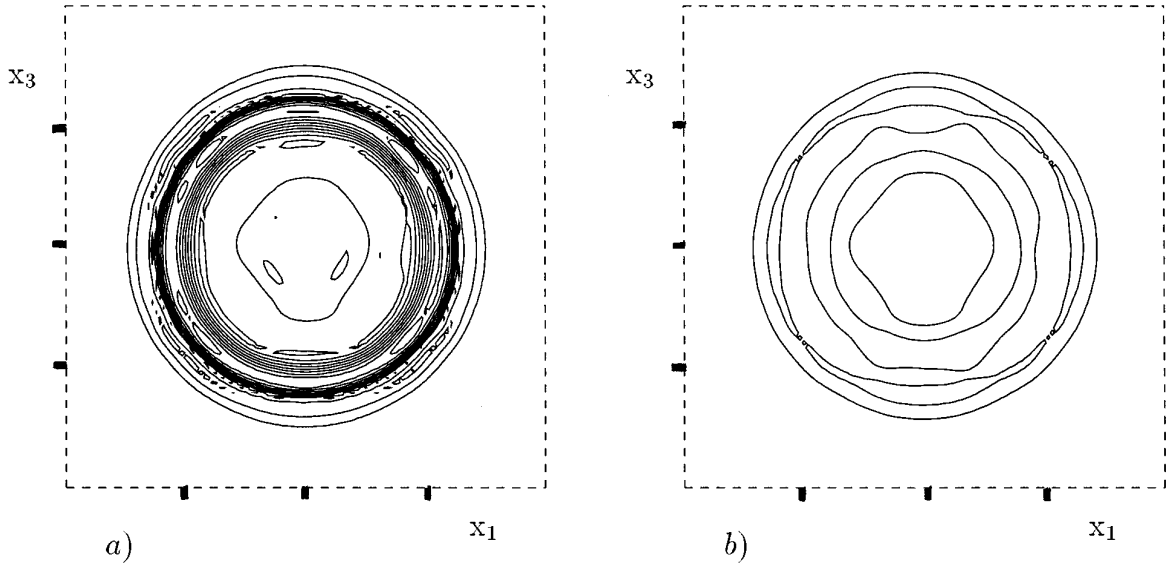
FIG. 9. Vorticity magnitude contour plots for a vortex ring impinging on a wall at Re = 1389 and $t = 48$. (Cartesian coordinates) (a) plane section crossing the center of the primary ring ($x_2 = 0.5$); (b) crossing the center of the secondary ring ($x_2 = 1.25$). —— positive values ($\Delta = \pm 0.05$). Tick marks are every $x_1, x_3 = 2r_0$.

It should be stressed that the same differences between Fig. 7a and the case $r_f = 4r_0$ of Fig. 7b have been evidenced also in [11]; however, the peak vorticities in the primary, secondary, and tertiary rings are the same in both cases.

As mentioned in the Introduction, although for some flows cylindrical coordinates are a "natural" choice, they can also be described in Cartesian coordinates, even if the rectangular domain introduces an unphysical $n = 4$ azimuthal perturbation. As an example we simulated the full three-dimensional normal collision of a vortex ring with a wall at Re $\simeq 1300$, both by the present method and by a primitive variable code in Cartesian coordinates (x_1, x_2, x_3). Owing to the low Reynolds number the resolution is quite coarse with a grid of $49 \times 49 \times 65$ for cylindrical coordinates and $65 \times 65 \times 65$ for Cartesian coordinates.

Figure 8 shows, by contour plots of the vorticity in vertical sections, that the shape, position, and strength of the vortical structures compare very well in both coordinate representations. However, horizontal sections through the center of the primary and secondary rings (Fig. 9) show that the computational perturbation introduced by the boundary deforms the toroidal axis of the ring. This deformation is more enhanced in the secondary ring (Fig. 9b), where the vorticity is weaker than in the primary. We wish to point out that the dynamics of the large structures is essentially the same in cylindrical and in Cartesian coordinates; however, in the latter case a study of azimuthal instabilities (as in [26]) would be meaningless.

5.3. Tripole Formation

In order to verify the correct treatment of the region at $r = 0$ the formation of a tripolar structure is simulated. From laboratory and computer experiments it has been shown [17] that a shielded monopolar vortex, when perturbed, produces a tripolar vortex. The physics of the formation of the structure and its characteristics are explained in [17], where a description of the numerical method used to compare the present results is also given.

The simulation has been performed in the $r - \theta$ plane where only one vorticity component (ω_z) exists. The initial vorticity profile is given by Eq. (9). The present results have been obtained for $\alpha = 3$, $\varrho = 1$, and a radial extent of the domain $r_f = 4$. The spatial resolution was for all runs 128×128 gridpoints respectively in the azimuthal and radial directions. In order to simulate the tripole formation a random perturbation, similar to that used in [17], has been superimposed to the vorticity distribution of Eq. (9).

The results show that the initially axisymmetric structure, soon loses the symmetry and, among the large numbers of the azimuthal wavenumbers of the initial perturbation, it selects the most unstable $m = 2$ mode. As the instability develops the central (positive) vortex becomes elliptical and along the longer sides the negative vorticity organizes in two satellite vortices. This configuration is steady and the structure (apart from viscous effects) rotates about the center of the vortex core in the sense of the positive vorticity (see Fig. 10).

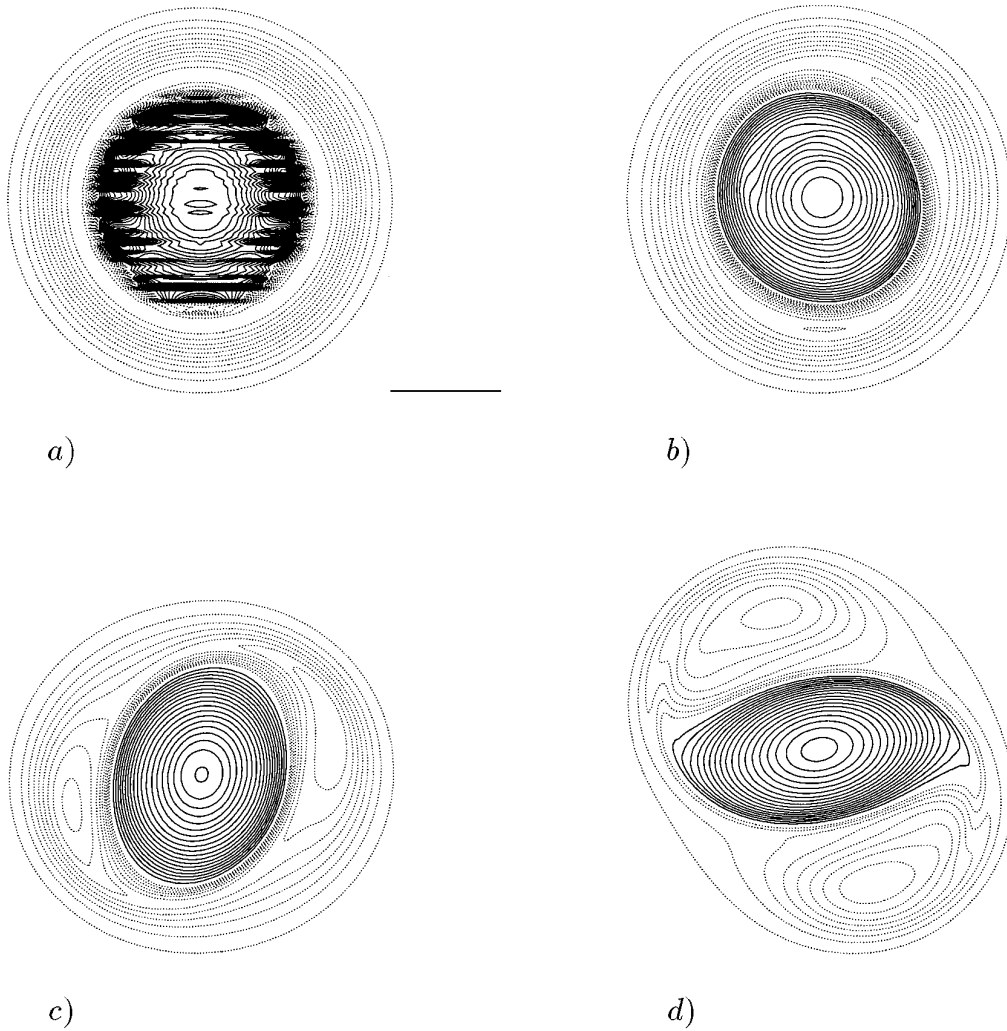Due to viscosity the peak vorticity slightly decreases in

FIG. 10. Vorticity contour plots of the tripole formation at Re = 2500. (a) $t = 0$, (b) $t = 20$, (c) $t = 40$, (d) $t = 60$. ———— positive values, $\cdots$ negative values ($\Delta = \pm 0.05$) (128×128 grid). The unit length is reported in the figure.

time and Fig. 11 shows how it changes with the Reynolds number. The same cases have been calculated by the method described in [17] and the results are compared in Fig. 11. Again the same considerations about the discrepancies at high Reynolds apply like in Section 5.1 for the axisymmetric free vortex ring. In fact, the numerical method of [17] conserves (in the limit Re $\rightarrow \infty$) circulation, energy and enstrophy and the correct energy transfer and the absence of unphysical vorticity is ensured [18]. However, the aim of this comparison was only to show that even for flows with the peak vorticity at the axis, the present method is successful.

5.4. Lamb Dipole

The previous examples have proved that the method works when there is a substantial axial velocity (vortex

ring) and axial vorticity (tripole) at the axis. Those cases, however, are all nearly axisymmetric and a motion perpendicular to the axis is absent. If the present numerical scheme has to deal with fully three-dimensional problems, it has to be able to simulate flows crossing the axis, since the most general three-dimensional flow will include also this possibility. The easiest way to provide such a flow is to allow a Lamb dipole to travel across the origin. The vorticity distribution for a Lamb dipole [27] is

$$\omega(\rho, \phi) = C J_1(k\rho)\sin \phi, \quad 0 \le \rho \le a, \qquad (11)$$

with C an amplitude parameter giving the intensity of the dipole and J_1 giving the first-order Bessel function of the first kind. The exterior flow being irrotational requires at the boundary $\rho = a = 1$, $J_1(ka) = 0$, that the first zero is
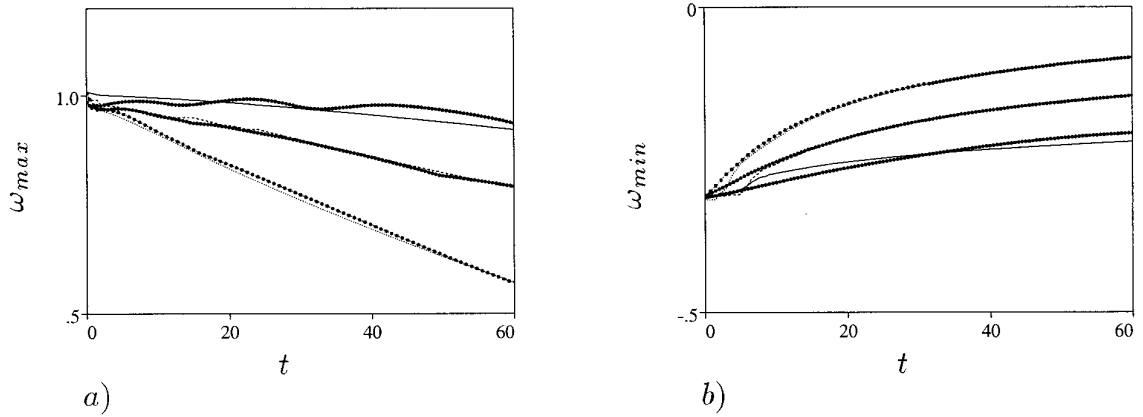
FIG. 11. Time evolution of the peak vorticities for the tripole formation. $\psi - \omega$ formulation: ——— Re = 2500; ––– Re = 1000, $\cdots$ Re = 500. Present scheme ●. (a) maximum vorticity, (b) minimum vorticity. Other run parameters are the same as Fig. 10.

given by $ka \simeq 3.83$. ρ and ϕ are respectively radial and azimuthal coordinates of a polar frame of reference with the origin in the center of the dipole. In these calculations it was assumed $C = 2k/J_0(ka)$ which gives a self-induced translation velocity of the isolated dipole equal to the unity. J_0 is again the zeroth-order Bessel function of the first kind.

The vorticity map corresponding to Eq. (11) is shown in Fig. 12a for a dipole centered at the axis. In the successive frames (Figs. 12b–c) it is displayed the motion of the structure towards the right due to the self-induced translation velocity, until the vortex has completely passed through the origin, without observing any distorsion of the vortex due to the discretization. A more severe test is given by the lower line of Fig. 12, showing the same phenomenon for a dipole initially off-axis.

For the dipole centered at the axis several resolutions have been used, ranging from 25×33 up to 385×513 grid points in the azimuthal and radial directions, respectively. Regarding the finest grid as an "exact" solution, the L_2-norm error has been computed for a flow configuration corresponding to Fig. 12b for which the largest vorticity gradients occur at $r = 0$. Figure 13 shows that in the range of effective use of the code (i.e., not too coarse grids) the second-order accuracy is retained both by azimuthal and radial velocity components. It should be stressed that this flow is not a good application for polar coordinates, since the cells become very small near the origin, velocities are high and the time step has to be kept very small due to stability constrains. This case, however, was run to show that, even within this severe test, the code maintained stability and accuracy.

A final central point that must be addressed, for the applicability of the method to full three-dimensional flows, is how much the time step has to be kept small for a general problem with some flow perpendicular to the axis. To give an estimate of the time step we use the turbulent pipe flow

by Eggels *et al.* [28] at $Re_c = U_c D/\nu = 6950$, with D the diameter of the pipe and U_c the centerline velocity. By a resolution of $96 \times 128 \times 128$ gridpoints, respectively, in the radial, azimuthal, and axial directions, numerical simulations were performed (Orlandi and Fatica, *personal communication*) with a $\Delta t = 2 \times 10^{-2} D/U_c$. The same flow was simulated in [28] with a grid $96 \times 128 \times 256$ (the axial discretization should not affect the stability) using $\Delta t = 8 \times 10^{-3} D/U_c$, but with a scheme that treated implicitly only the terms containing azimuthal derivatives. On the other hand, the physics of the flow also imposes restrictions on the maximum time step in order to capture the features of the smallest scales. Eggels *et al.* [28] estimated the Kolmogorov time scale for the above flow to be $\Delta t \simeq 2 \times 10^{-1} D/U_c$; therefore, the time step imposed by stability constraints is not too small.

CONCLUSIONS

Highly accurate spectral methods are extensively used for the simulation of flows in Cartesian coordinates. When curvilinear grids are required standard spectral methods are unusable and finite-differences can be efficiently employed. Finite-differences are less accurate than spectral methods; however, Choi *et al.* [10] showed comparable accuracy between a second-order and spectral algorithm with the same number of points when it is sufficient to describe velocity fluctuations. On the other hand, it is necessary to double the grid in all directions to adequately resolve the vorticity fluctuations.

The current study presents a second-order finite-difference scheme for the calculation of incompressible flows in cylindrical coordinates. The coordinate system is singular at $r = 0$; this difficulty is bypassed by the introduction of the radial flux $q_r = r \cdot v_r$ and the use of a staggered grid. The qualities of the method have been evaluated by com-
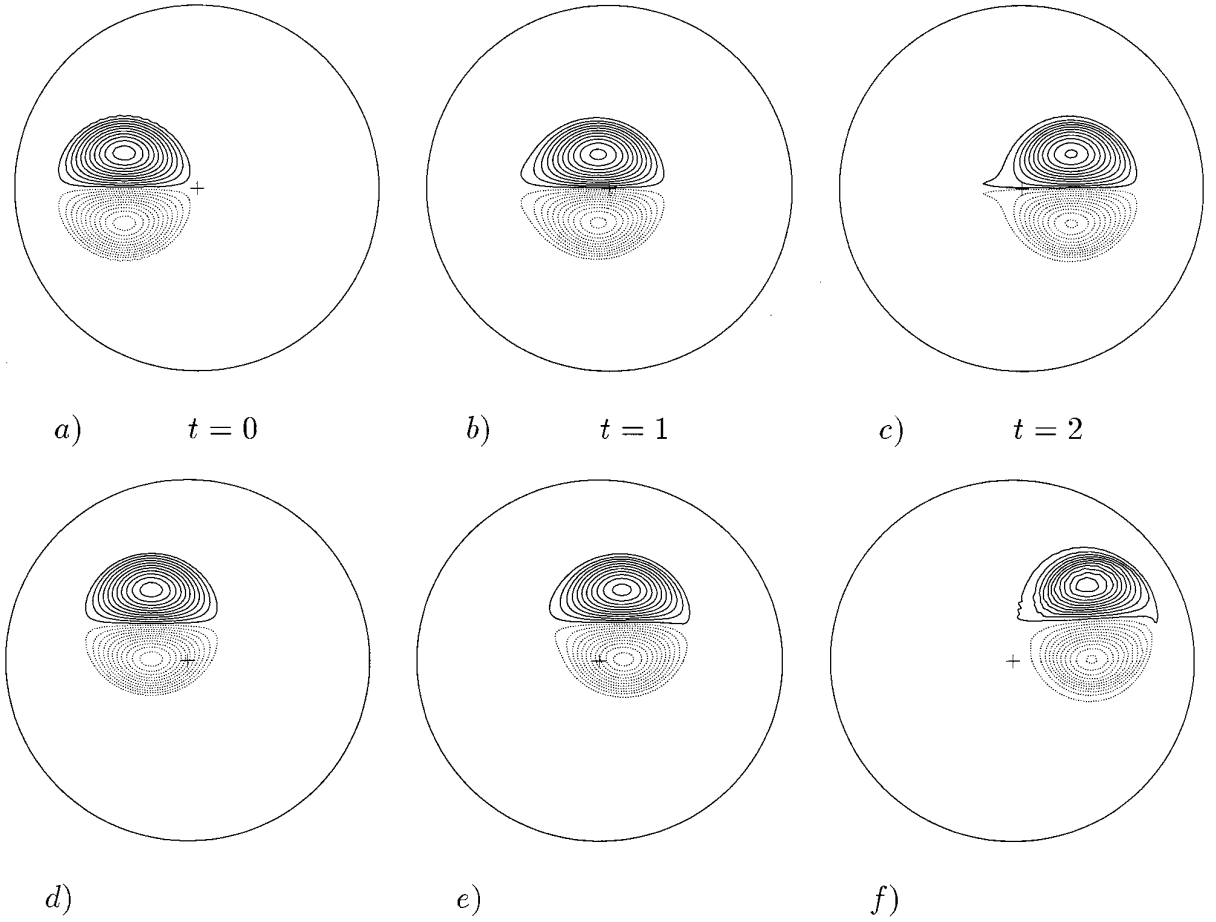
FIG. 12. Vorticity maps of the Lamb dipole at Re = 1000. (a), (b), (c) centered case, (d), (e), (f) eccentric case: ——— positive, · · · negative values, $\Delta = \pm 1$. The cross in the plots indicates the coordinates origin. Size of the dipole $a = 1$, radius of the domain $r_f = 2.5$, free-slip wall at the boundary, (97 × 129) grid in the azimuthal and radial directions.
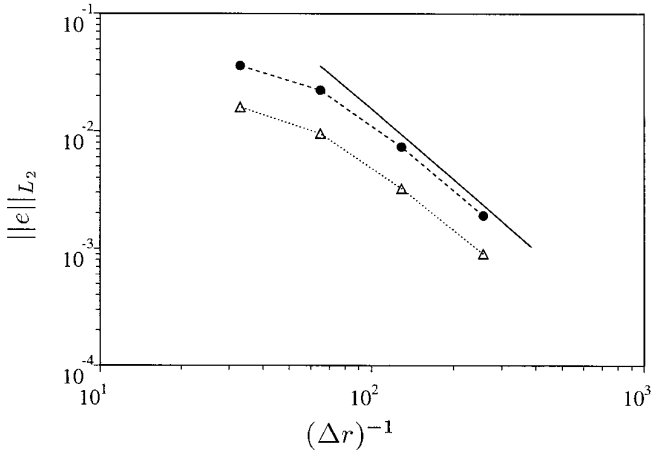

FIG. 13. Accuracy check for the radial ● and azimuthal △ velocity components vs the grid spacing. ——— slope-2 for comparison. (The radial and azimuthal grid spacing are refined in the same way in each run).

paring the results for two-dimensional, axisymmetric, and three-dimensional flows with those obtained by other numerical methods, experiments, and theory. The comparison was satisfactory in all cases. Results obtained for two-dimensional and axisymmetric flows have shown, at high Reynolds numbers, small differences. As stated by Arakawa [18] this is due to the lack of conservation of some quadratic invariant (enstrophy for two-dimensional and $\int (\omega/r)^2 \, dS$ for axisymmetric flow). These small differences are easily eliminated by slightly increasing the spatial resolution; however, the present scheme has been mainly designed for full three-dimensional flows, where this problem was not faced since those invariant are not conserved.

By the two examples of vortex dynamics in the $(r - \theta)$–plane (Sections 5.3, 5.4), we have shown that this numerical method is suitable for the simulation of those experiments performed in rotating tanks. Of course, for a close correspondence with the experiments it needs to be simulated not only for the effect of the lower and circumfer-

ential solid boundaries (already possible by the present scheme), but also for the upper free surface. For low rotation rates of the tank the free surface can be easily approximated by a rigid free-slip wall. On the contrary, for high rotation rates the deformations of the surface become important and these would require much more work.

APPENDIX

A1. *Boundary Conditions*

In Section 3 it has been mentioned that $q_i^{l+1} = \hat{q}_i + O(\Delta t^2)$. To prove this statement we follow the procedure described in [21]. Regarding $\hat{q}_i$ as an approximation to the quantity q_i^*, continuous in time, it is required that q_i^* satisfy the conditions

$$\frac{\partial q_i^*}{\partial t} = -\mathcal{G}_i p^* + H_i^* + \frac{1}{\text{Re}} \mathbf{A}_i q_i^*,$$

$$q_i^{l+1} = q_i^*(t_{l+1}), \quad p^{l+1} = p^*(t_{l+1}),$$

where for brevity it has been indicated by $\mathbf{A}_i$, the operator for the viscous terms ($\mathbf{A}_i = A_{i\theta} + A_{ir} + A_{iz}$) of Eq. (1a). For the generic time step we can write

$$\hat{q}_i \approx q_i^*(t_{l+1}) = q_i^*(t_l) + \frac{\partial q_i^*}{\partial t}\bigg|_{t_l} \Delta t + O((\Delta t)^2)$$

$$= q_i^*(t_l) + \left(-\mathcal{G}_i p^* + H_i^* + \frac{1}{\Re} \mathbf{A}_i q_i^*\right)\bigg|_{tl} \Delta t + O((\Delta t)^2).$$

Since $q_i^{l+1} = q_i^*(t_{l+1})$ and $p^{l+1} = p^*(t_{l+1})$ it follows that

$$\hat{q}_i = q_i^l + \left(-\mathcal{G}_i p^l + H_i^l + \frac{1}{\text{Re}} \mathbf{A}_i q_i^l\right) \Delta t + O((\Delta t)^2)$$

$$= q_i^l + \frac{\partial q_i}{\partial t}\bigg|_{t_l} \Delta t + O((\Delta t)^2),$$

so that

$$\hat{q}_i = q_i^{l+1} + O((\Delta t)^2).$$

ACKNOWLEDGMENTS

REFERENCES

1. A. Wray and Y. Hussaini, *AIAA Paper* **80-0275,** Pasadena, CA, 1980 (unpublished).

2. P. Moin and J. Kim, *J. Fluid Mech.* **118,** 159 (1982).

3. M. M. Rogers, and R. D. Moser, *J. Fluid Mech.* **243,** 183 (1992).

4. V. M. Melander, F. Hussain, and A. Basu, "Breakdown of a Circular Jet into Turbulence," in *Proceedings, 8th Symp. on Turb. Shear Flows, Munich, 1991* (unpublished).

5. S. K. Stanaway, B. J. Cantwell, and P. R. Spalart, *Ph.D. thesis,* NASA TM 101041, 1988 (unpublished).

6. A. Leonard and A. Wray, "A New Numerical Method for the Simulation of Three-Dimensional Flow in a Pipe," in *Fourth Int. Conf. on Numer. Methods in Fluid Dyn., Colorado, Lecture Notes in Physics,* Vol. 135, p. 335 (Springer-Verlag, New York, 1975).

7. J. C. Buell and I. Catton, *J. Heat Transfer* **105,** 255 (1983).

8. J. G. M. Eggels, *Ph.D. thesis*, Delft University of Tech., 1994 (unpublished).

9. M. M. Rai, and P. Moin, *J. Comput. Phys.* **96,** 15 (1991).

10. H. Choi, P. Moin, and J. Kim, *Ph.D. thesis* TF-55, Stanford University, 1992 (unpublished).

11. P. Orlandi and R. Verzicco, *J. Fluid Mech.* **256,** 615 (1993).

12. R. Verzicco and P. Orlandi, *Phys. Fluids* **6,** 751 (1994).

13. U. Schumann, *J. Comput. Phys.* **18,** 376 (1975).

14. S. E. Widnall and C. Y. Tsai, *Phil. Trans. R. Soc. London A* **287,** 273 (1977).

15. P. G. Saffman, *J. Fluid Mech.* **84,** 625 (1978).

16. J. D. A. Walker, C. R. Smith, A. W. Cerra, and J. L. Doligaski, *J. Fluid Mech.* **181,** 99 (1987).

17. P. Orlandi and G. J. F. van Heijst, *Fluid Dyn. Res.* **9,** 179 (1992).

18. A. Arakawa, *J. Comput. Phys.* **1,** 119 (1966).

19. A. Grammelvedt, *Mon. Weather Rev.* **97**(5), 384 (1969).

20. K. Horiuti, *J. Comput. Phys.* **71,** 343 (1987).

21. J. Kim and P. Moin, *J. Comput. Phys.* **59,** 308 (1985).

22. R. M. Beam and R. F. Warming, *J. Comput. Phys.* **22,** 87 (1976).

23. P. R. Spalart, R. D. Moser, and M. M. Rogers, *J. Comput. Phys.* **96,** 297 (1991).

24. L. E. Fraenkel, *J. Fluid Mech.* **51,** 119 (1972).

25. P. G. Saffman, *Stud. Appl. Math.* **49**(4), 371 (1970).

26. K. Shariff, R. Verzicco, and P. Orlandi, *J. Fluid Mech.* **279,** 351 (1994).

27. Sir H. Lamb, *Hydrodynamics* (Dover, New York, 1932).

28. J. G. M. Eggels, F. Unger, M. H. Weiss, J. Westerweel, R. T. Adrian, R. Friedrich, and F. T. M. Nieuwstadt, *J. Fluid Mech.* **268,** 175 (1994).